The Optical Properties of Equatorial Cirrus in the Pilot Radiation Observation Experiment

C. M. R. Platt, S. A. Young, P. Manson, G. R. Patterson, and S. Marsden
CSIRO, Division of Atmospheric Research
Aspendale, Victoria, Australia

Introduction

The development of a sensitive filter radiometer for the Atmospheric Radiation Measurement (ARM) Program has been reported by Platt et al. (1994, 1995). The aim was to develop a reliable and fast instrument that could be used alongside a lidar to obtain near realtime optical properties of clouds, particularly high ice clouds, as they drifted over an ARM Cloud and Radiation Testbed (CART) site allowing calculation of the radiation divergence in the atmosphere over the site. Obtaining cloud optical properties by the lidar/radiometer, or LIRAD, method was described by Platt (1979) and Platt et al. (1987); the latter paper also describes a year's data on mid-latitude cirrus.

The optical properties of equatorial cirrus (i.e., cirrus within a few degrees of the equator) have hardly been studied at all. The same is true of tropical cirrus, although a few observations have been reported by Davis (1971) and Platt et al. (1984).

The ARM Pilot Radiation Observation Experiment (PROBE) took place in the southern summer of 1992-93 as part of the Tropical Ocean Global Atmosphere (TOGA) Coupled Ocean Atmospheric Response Experiment (COARE), and was sited at Kavieng, New Ireland, Papua New Guinea (2.5°S latitude, 152°E longitude). The CSIRO Division of Atmospheric Research (DAR) lidar and radiometer was operated at Kavieng for about three weeks in January-February 1993. During that time, several extensive cirrus clouds were studied, particularly during periods when there was little cumulus or altocumulus developing in the line of sight. This article describes these observations, the analysis method used, and a summary of the results.

Observations

Observations were made on cirrus clouds whenever the opportunity arose during daylight hours and on a few evenings. Extensive cirrus layers were observed on January 24th, 26th, and 29th and February 3rd and 4th. Cirrus were also studied on some other days for brief periods.

The equipment consisted of the CSIRO three wavelength lidar, operating at 0.53 micron, and two radiometers, the CSIRO DAR MARK II radiometer detecting in a band centered at 10.84 micron wavelength and the ARM cooled HgCdTe radiometer detecting at three wavelengths centered at 8.62, 10.86, and 12.04 microns. At Kavieng, observations were made both at 8.62 and 10.86 microns. The CSIRO radiometer was used on January 24th and February 3rd and 4th when liquid nitrogen was unavailable. It was also operated simultaneously with the ARM radiometer on January 29th. A detailed comparison of the performances of these radiometers was given in Platt et al. (1995). The ARM radiometer was found to be markedly superior.

The lidar and radiometer were both operated vertically and both with fields of view of about 8 mrad, corresponding to a cloud area sampled of about 130 m at 16-km altitude, and 80 m at 10 km. The lidar fired a number of shots at a frequency of 10 hz at intervals of 30 seconds, the number of profiles varied depending on the cloud height and optical depth. The radiometers recorded continuously with time constants of 5 seconds for the CSIRO MARK II and 1 second for the ARM. The Lidar and radiometer clock times were compared closely.

Observations were made when there was cirrus above the site without intervening clouds. Lidar observations were obtained at times also on middle-level altocumulus as well as cumulus, but the large changes in dynamic range in backscatter caused problems and the lidar was frequently turned off when low clouds intervened. A radiance trace for one day is shown in Figure 1. Periods of cumulus in Figure 1 are clearly identifiable as an increase in radiance to about $4.7 Wm^{-2}sr^{-1}$ at 10.84 microns for "black" cumulus.

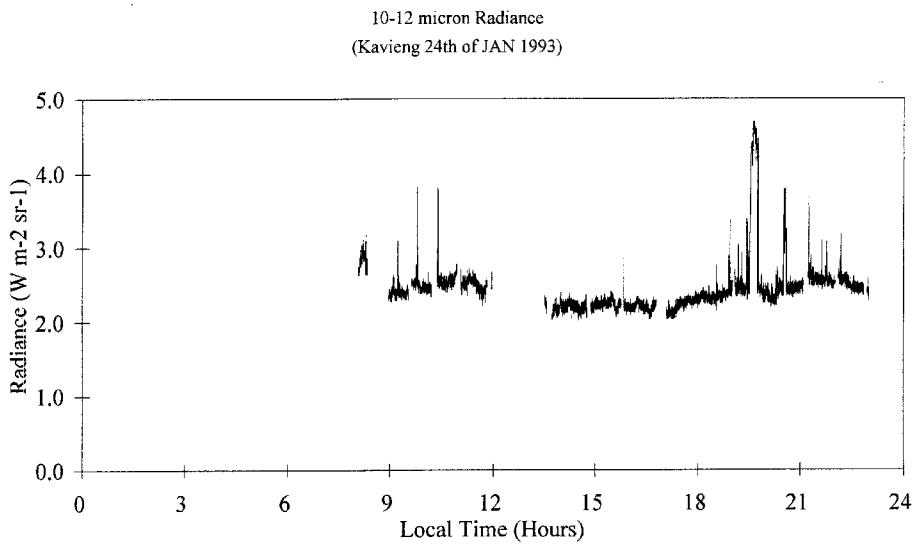

Figure 1. Radiance output for one day using the CSIRO radiometer. High peaks in the radiance represent cumulus episodes.

Calibration

In order to calculate the optical properties of the clouds accurately, both lidar and radiometers needed to be well calibrated. The lidar was calibrated against Rayleigh scatter at an altitude which was judged to be aerosol free by a method developed by Young (1995). Each lidar profile was obtained by averaging a sufficient number of shots to obtain a profile that had enough signal-to-noise ratio both below and above the cloud (when semitransparent). In these regions the range-corrected lidar signal was fitted to a reference molecular backscatter signal that was obtained from suitably interpolated radiosonde profiles. By fitting the lidar profile to the molecular profile above and below the cloud layer the cloud transmittance and hence the visible optical depth could also be calculated. As radiosonde data were only available below about 18 km, climatological or satellite data were used above this height. One difficulty with using this method with high clouds at Kavieng was the strong scattering from the Mt. Pinatubo volcanic aerosol layer above the clouds which made any fitting of the lidar profile to a molecular profile in this region invalid. A solution to this problem was found in these cases by replacing the molecular reference profile with a reference profile produced by averaging several thousand cloud-free lidar signals. Each profile was calibrated against the reference profile, thus allowing an assessment of data quality by studying the magnitude of the means and standard deviations in the fitting parameters.

The infrared radiometers were calibrated against liquid nitrogen, or ice water, when liquid N_2 was not available. Difficulties were experienced in the accurate calibration of the CSIRO radiometer which had to be operated outside the sea-container laboratory. Fluctuating ambient temperatures caused large drifts in the electronics gain and draughts caused the build-up of condensed water or ice above the liquid N_2, thus elevating the measured radiance. However, careful and frequent calibrations reduced uncertainties to a controllable level. The incoming signals were chopped against two reference blackbodies maintained at 40°C that filled half the apertures, a design common to both radiometers. The radiometers were calibrated against an external blackbody at temperatures around 40°C to check at what temperature the output signal fell to zero in practice. Because of small misalignments, this temperature was usually not exactly 40°C. However, knowledge of the exact "cross-over" temperature was sufficient for a complete calibration. Subsequent closer examination of calibration curves revealed some non-linearities in the ARM radiometer, but only at high calibration temperatures. These were taken into account in the calibrations.

Theory

The lidar equation can be written

$$\gamma(\pi) = (k/2\eta)\left[1-\exp\left(-(2\alpha\eta)\log\left(\frac{1}{1-\epsilon}\right)\right)\right] \qquad (1)$$

where k is the backscatter to extinction ratio, η is a multiple scattering factor that effectively reduces the extinction, ϵ is the infrared emittance, and α is the ratio between visible lidar extinction and infrared absorption optical depths. It can be seen that when $\epsilon = 1, \gamma(\pi) = (k/2\eta)$

The infrared emittance can be related to the infrared absorption optical depth δ_a by the relation

$$\epsilon = 1 - \exp(-\delta a) \quad (2)$$

where scattering terms are neglected.

Analysis

The basis of the analysis of the data was the method reported by Platt et al. (1987)-the standard lidar/radiometer (LIRAD) technique. However, one refinement was the use of water vapor data measured by the microwave radiometer at the Environmental Technology Laboratory of the National Oceanic and Atmospheric Administration which supplied a continuous output of the water vapor path over the site. Profiles of temperature and humidity were also available every six hours from radiosonde data. These data allowed a continuous update of the water vapor emission and transmittance of radiation to the radiometer, instead of relying on the simple linear interpolation between morning and evening radiosondes that had been used in previous experiments. The water vapor transmittance was obtained as follows. The water vapor radiances were calculated from the radiosonde data for the whole period using a radiative transfer equation for a range of water vapor continuum absorption coefficients, allowing also for water vapor line absorption (Platt et al. 1984). The radiances were then compared with clear-sky radiances observed at similar times. The transmittance was calculated from the radiance that was closest to the observed radiance. Apparent changes in water vapor continuum absorption were attributed to changes in aerosol absorption different from the nominal aerosol optical depth of 0.04 (Platt et al. 1984).

In order to utilize the observed microwave water vapor path (w), w was normalized to the observed radiance when the sky overhead was clear. Intermediate radiance's were then related to the measure values of w. If necessary, radiance's were interpolated between observation points. The water vapor transmittance was then related to the corresponding radiance. This was done for the Kavieng data by regressing all theoretically calculated radiance's against corresponding transmittances for the total period of Kavieng radiosonde observations. The resultant plot is shown in Figure 2.

The standard LIRAD technique utilized the retrieved lidar profile of backscatter coefficient to calculate a cloud radiance, with the radiosonde data interpolated between the times of two radio soundings. The radiance calculation used a simple non-scattering radiative transfer equation, with spectral blackbody radiances assigned to different cloud levels and a constant ratio (ξ) assumed between cloud absorption coefficient and lidar backscatter coefficient. The measured surface radiance was corrected for water vapor emission and absorption and then compared with the calculated value. The constant ξ was then adjusted until agreement between the measured and observed radiances was obtained. The cloud infrared emittance and transmittance was then calculated. Corrections were made for first order effects of both scattering within the cloud and reflection of upwelling surface radiation.

The cloud backscatter coefficients were corrected for attenuation by a forward integration technique (Platt 1979) using a cloud backscatter to extinction ratio $k/2\eta$ (see Equation 1) derived from the lidar integrated backscatter $\gamma'(\pi)$ when the cloud became optically thick and the emittance tended to unity. The cloud visible optical depth could thus also be derived. The cloud infrared optical depth is similarly derived from the infrared emittance. The uncertainties in both the visible and infrared optical depth calculations are known to become greater as the cloud becomes optically thick. A relevant error analysis was given by Platt (1979).

Results and Discussion

Preliminary results were reported in Platt et al. (1995), where it was shown that the lidar integrated backscatter $\gamma'(\pi)$ correlated well with the infrared emittance in one limited period. Here we present a more complete set of results showing the behaviors of cloud depth, infrared emittance, and integrated backscatter.

The depths of the cirrus clouds observed over Kavieng are shown in Figure 3. They were consistently large, in the region of 3 or 4 km on average. These depths were considerably greater than those measured either at Darwin or in mid-latitudes (Platt et al. 1984, 1987). The Darwin points are also shown for comparison in Figure 3. The clouds were generally multi-layered although they often

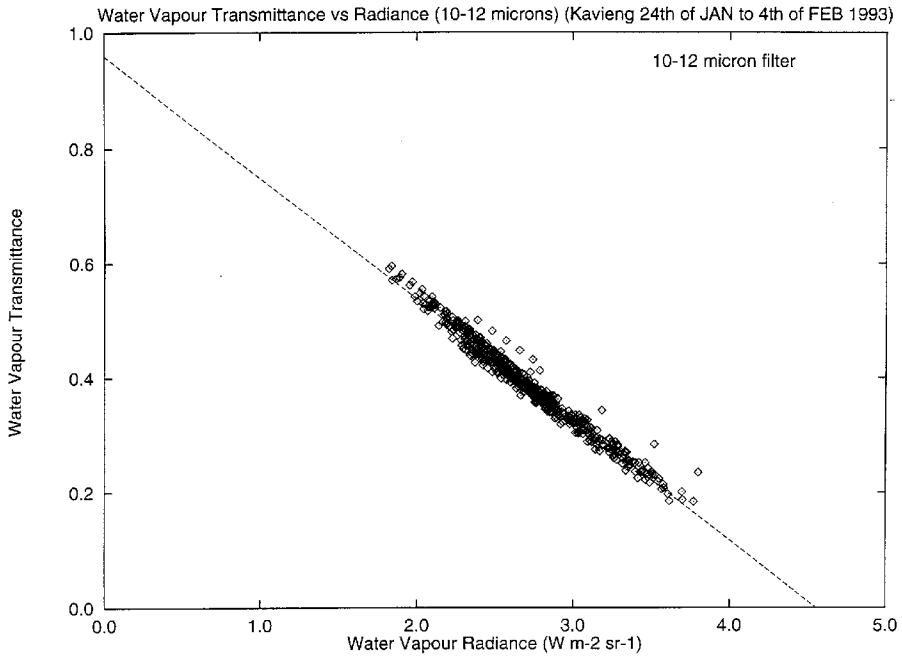

Figure 2. Plot of the water vapor transmittance from the cirrus clouds to the surface against water vapor radiance.

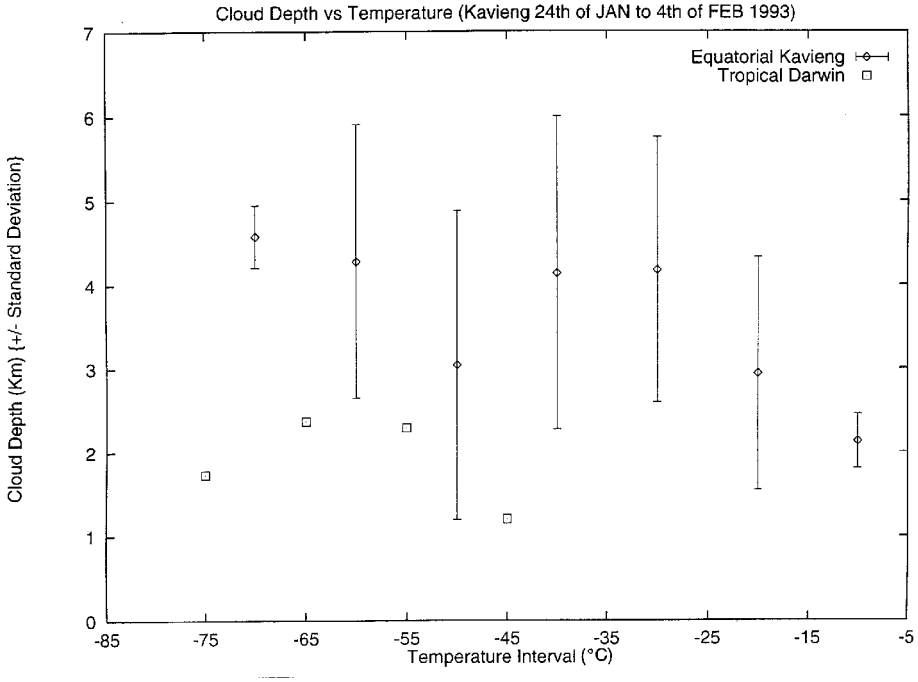

Figure 3. Plot of cirrus cloud depth against mid-cloud temperature. The bars represent the variability in cloud depth.

consolidated during daylight hours, descended, and became optically denser. These deep, multi-layer clouds would indicate deep layers of moist air below the tropopause, presumably due to water vapor ADVECTED from thunderstorms or mesoscale systems.

The beam emittance is shown in Figure 4 where the frequencies of various emittances are displayed. The emittance peaks at 0.2 to 0.3 which again is different from both Darwin and the mid-latitude cases for synoptic cirrus and values were more typical of anvil cirrus (e.g., Platt et al. 1984). In the fomer cases, the cirrus frequency decreased systematically with emittance.

Plots of integrated backscatter (see Equation 1) versus infrared emittance are shown in Figures 5 and 6 for the temperature regions of -35°C to -75°C and -5°C to -35°C, respectively. These have a characteristic shape typical of the Darwin and mid-latitude clouds. Values of $k/2\eta$ have been deduced for each temperature range and are shown plotted against temperature in Figure 7. In this case, the values are very similar to the Aspendale summer values, but lower than those at Darwin, where all points of $\gamma'(\pi)$ versus ϵ tended to lie on the same line. This behavior in the integrated backscatter in equatorial cirrus is encouraging in that the crystal composition of clouds at various latitudes may be quite similar. There are, of course, exceptions, as shown in Figure 7, that need further investigation.

Conclusions

The data on equatorial cirrus presented here are quite unique. As intended in the original aims of PROBE, the data form an initial resource for climate modelling of cirrus over the warm pool areas of the Tropical West Pacific region. The data will first be used in a study, in collaboration with G. L. Stephens, to determine the radiation budget of and heating in the cirrus clouds. This forms a study that is central to the general ARM thrust. The data will be available from in the PROBE section of the TOGA COARE archive. The visible optical depths and lidar linear depolarization ratios of the clouds for some selected clouds have also been determined and will soon be available.

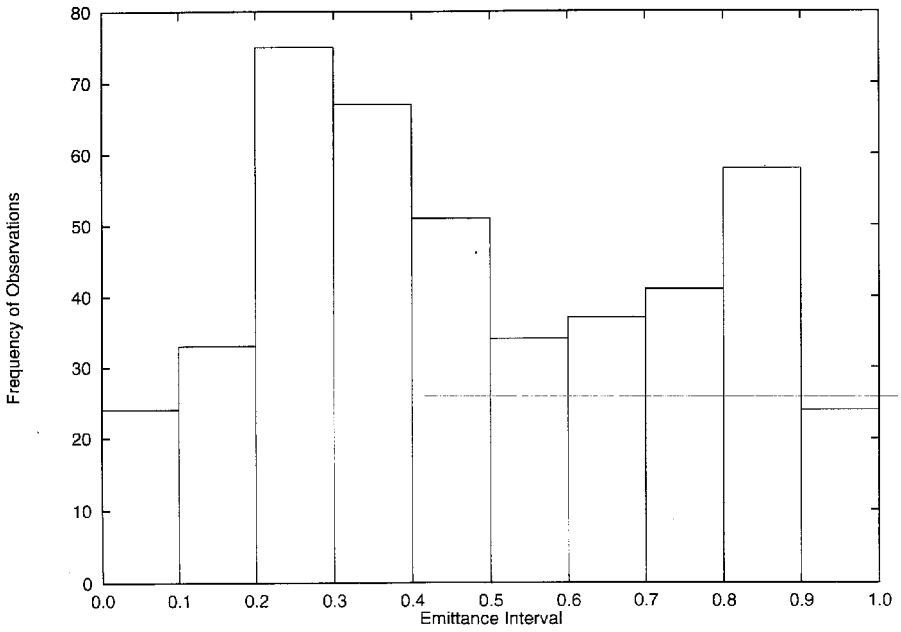

Figure 4. Frequency of observation of beam emittance of a given value.

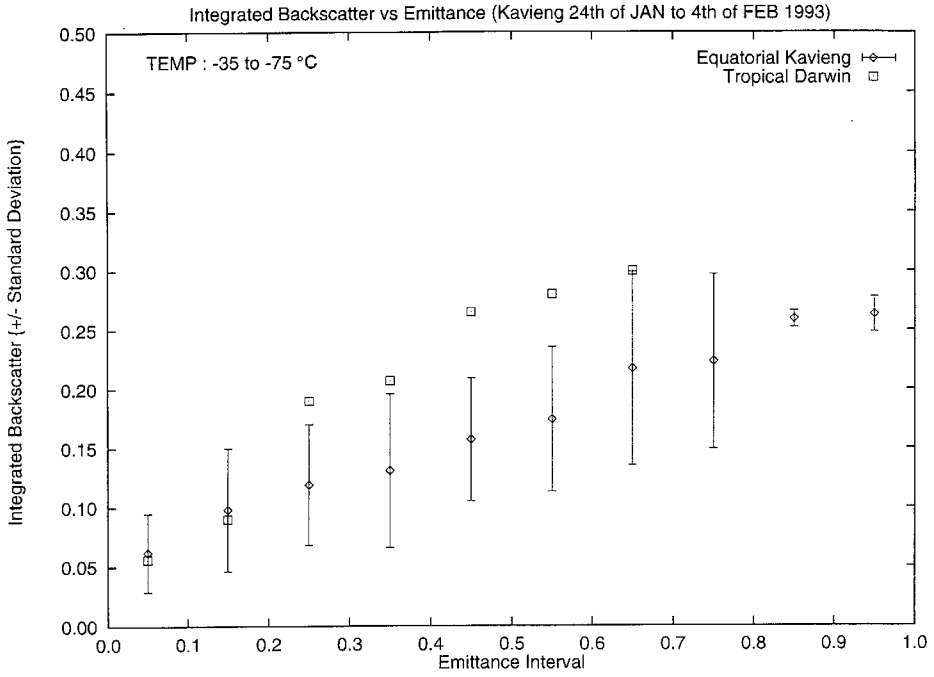

Figure 5. A plot of integrated backscatter against infrared emittance for the temperature range shown. Bars represent variability in observed backscatter, -35 to -75°C.

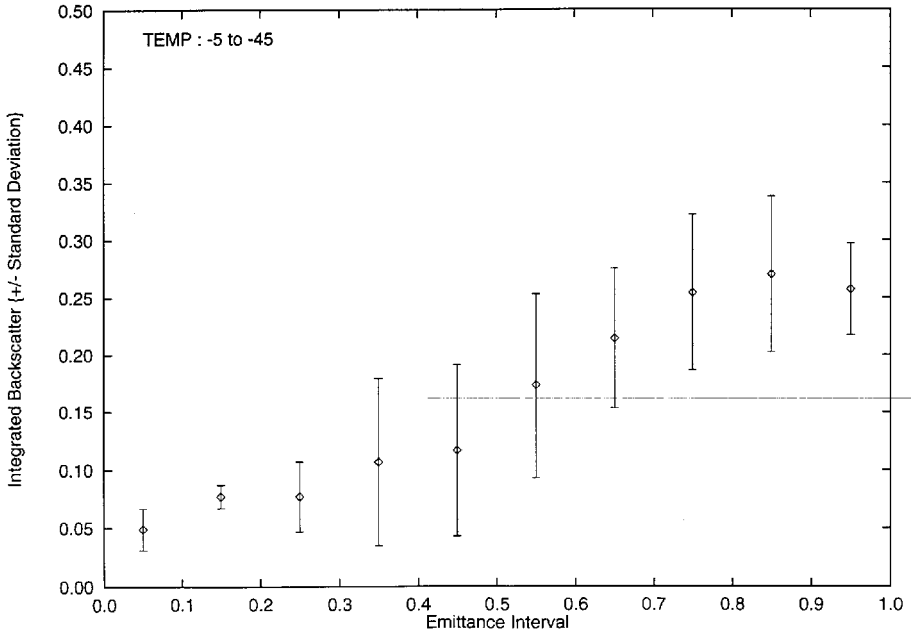

Figure 6. A plot of integrated backscatter against infrared emittance for the temperature range shown. Bars represent variability in observed backscatter, -5 to -45°C.

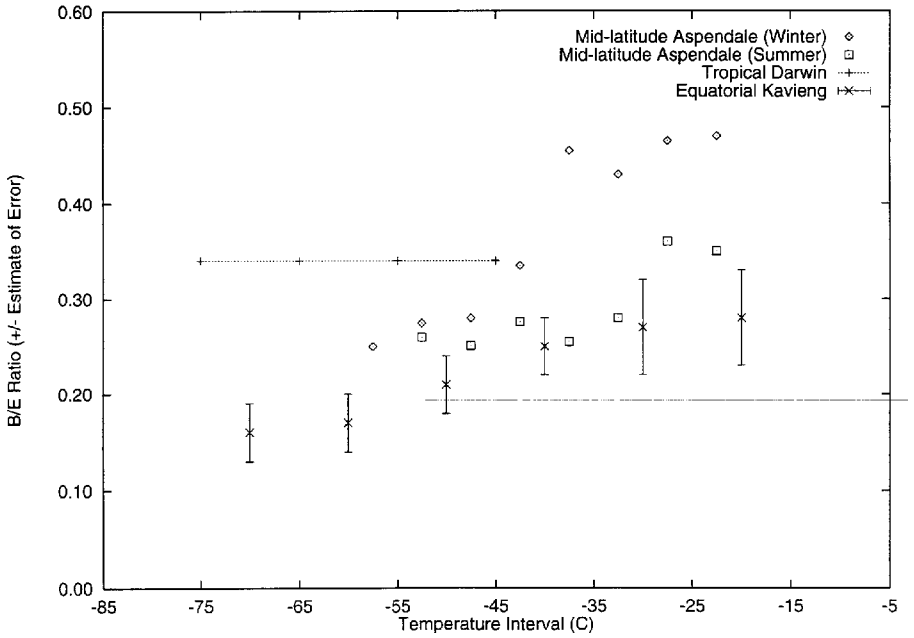

Figure 7. Plot of the isotropic backscatter to extinction ratio modified by multiple scatter of against mid-cloud temperature.

The results point to the desirability of obtaining further data on equatorial cirrus. Particularly, data is needed with high-power lidar and radiometry-and interferometry. It would also be desirable to have millimeter radar. The best mode for such data might be a campaign-type experiment at one of the new tropical Western Pacific CART sites, when they are installed.

References

Davis, P. A. 1971. Applications of an airborne ruby lidar during a BOMEX program of cirrus observations, *J. Appl. Meteor.*, **10**, 1314-1323.

Platt, C. M. R. 1979. Remote sounding of high clouds I: Calculation of visible and infrared optical properties from lidar and radiometer measurements, *J. Appl. Meteor.*, **18**, 1130-1143.

Platt, C. M. R., A. C. Dilley, J. D. Scott, I. J. Barton, and G. L. Stephens. 1984. Remote sounding of high clouds. V: Infrared properties and structures of tropical thunderstorm anvils, *J. Appl. Meteor.*, **23**, 1296-1308.

Platt, C. M. R., J. C. Scott, and A. C. Dilley. 1987. Remote sounding of high clouds VI: Optical properties of mid-latitude and tropical cirrus, J. Atmos. Sci., **44**, 729-747.

Platt, C. M. R., S. A. Young, P. J. Manson, and G. R. Patterson. 1995. Observations of tropical cirrus properties in the PROBE using lidar and the CSIRO ARM filter radiometer, *Prob. 4th ARM Sci. Team. Mtg*, (in Press).

Young, S. A. 1995. Analysis of lidar backscatter profiles in optically thin clouds, *App. Opt.*, **34**, 7019-7031.